Science Robotics
AAAS

robotics.sciencemag.org/cgi/content/full/4/32/eaax0613/DC1

Supplementary Materials for

A microrobotic system guided by photoacoustic computed tomography for targeted navigation in intestines in vivo

Zhiguang Wu, Lei Li, Yiran Yang, Peng Hu, Yang Li, So-Yoon Yang, Lihong V. Wang*, Wei Gao*

*Corresponding author. Email: lvw@caltech.edu (L.V.W.); weigao@caltech.edu (W.G.)

Published 24 July 2019, *Sci. Robot.* **4**, eaax0613 (2019)
DOI: 10.1126/scirobotics.aax0613

The PDF file includes:

Other Supplementary Material for this manuscript includes the following:

(available at robotics.sciencemag.org/cgi/content/full/4/32/eaax0613/DC1)

Movie S1 (.avi format). Animated illustration of the PAMR in vivo.
Movie S2 (.avi format). PA imaging of the migration of a MC in model intestines.
Movie S3 (.avi format). NIR-triggered destruction of the MC and activated autonomous propulsion of the ingestible micromotors.
Movie S4 (.avi format). Propulsion of the micromotors in biofluids.
Movie S5 (.avi format). PA imaging of the MCs in vivo for 7.5 hours.
Movie S6 (.avi format). PA imaging of the migration of an MC toward a model colon tumor in intestines.

Text S1. Small-animal whole-body imaging modalities and photoacoustic computed tomography

Previously, small-animal whole-body imaging has typically relied on non-optical approaches, including X-ray computed tomography (X-ray CT), magnetic resonance imaging (MRI), positron emission tomography (PET) or single-photon emission computed tomography (SPECT), and ultrasound imaging (USI) (*16*). Although these techniques provide deep penetration, they suffer from significant limitations. For example, microscopic MRI requires a long data acquisition time, ranging from seconds to minutes, too slow for imaging dynamics (*50*, *51*). More importantly, MRI, requiring a strong magnetic field, is incompatible with magnetically driven or guided micromotors (*5*). X-ray CT has poor contrast of the micromotors made of biocompatible/biodegradable metals (*15*, *52*). PET/SPECT alone suffers from poor spatial resolution. In addition, X-ray CT and PET/SPECT employ ionizing radiation, which inhibits longitudinal monitoring (*53*). USI does not image extravascular molecular contrasts (*54*). In addition, the MCs described in this manuscript are mainly by mass composed of gelatin, which has almost the same acoustic impedance as soft tissue (*55*). Thus, USI cannot image the MCs with sufficient contrast *in vivo*. Optical imaging uses non-carcinogenic electromagnetic waves to provide extraordinary molecular contrasts with either endogenous or exogenous agents at high spatiotemporal resolution. Unfortunately, the strong optical scattering of tissue hampers the application of conventional optical imaging technologies to small-animal whole body imaging at high spatial resolution (*16*). To date, photoacoustic tomography (PAT) is the only optical imaging modality that breaks the optical diffusion limit (*17*) on penetration and achieves high-resolution imaging in deep tissues with optical contrasts.

As a major incarnation of PAT, photoacoustic computed tomography (PACT) has attained high spatiotemporal resolution, deep penetration, and anatomical and molecular contrasts. Typically, when implemented in PACT, a laser pulse broadly illuminates the whole tissue to be imaged. As photons propagate inside the tissue, some are absorbed by molecules, and their energy is partially or completely converted into heat, creating a temperature rise through nonradiative relaxation. The local temperature rise induces a pressure rise through thermoelastic expansion. The pressure rise propagates, at a speed of roughly 1500 m s^{-1}, inside the tissue as a photoacoustic wave, and is detected outside the tissue by an ultrasonic transducer or transducer array. The detected photoacoustic signals are processed by a computer to form an image, which maps the original optical energy deposition in the biological tissue. Because ultrasound scattering in soft tissue is about three orders of magnitude weaker than light scattering on a per unit path length basis in the ultrasonic frequency of interest, PACT has achieved superb spatial resolution at depths by detecting ultrasound.

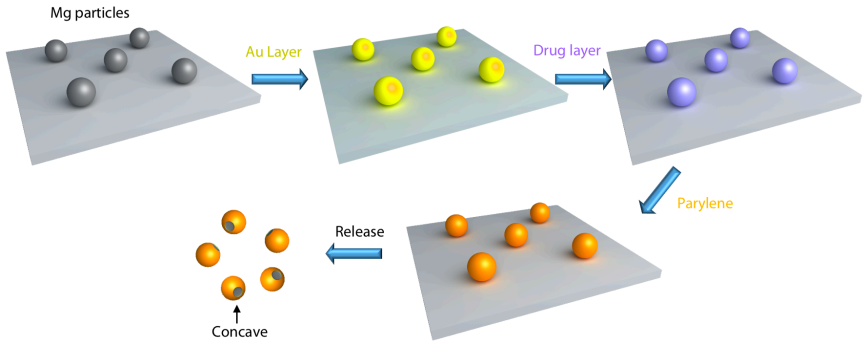

Fig. S1. The fabrication flow of the ingestible micromotors.

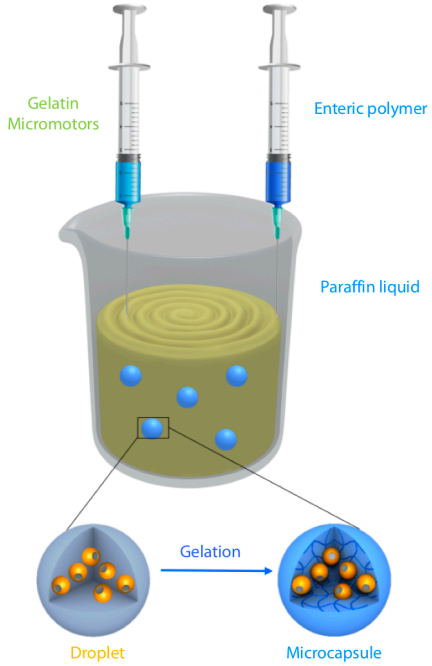

Fig. S2. The preparation of the MCs.

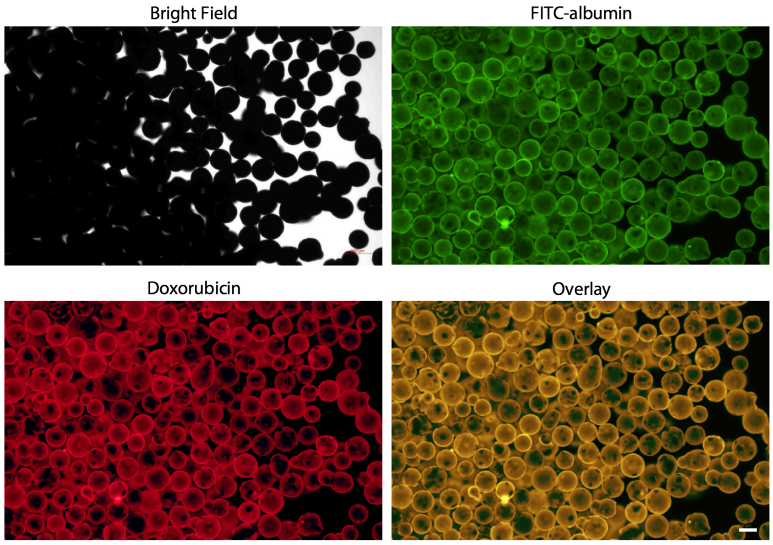

Fig. S3. Bright field and fluorescence microscopic images of the micromotors confirming the successful drug loading in micromotors. Scale bar, 20 μm.

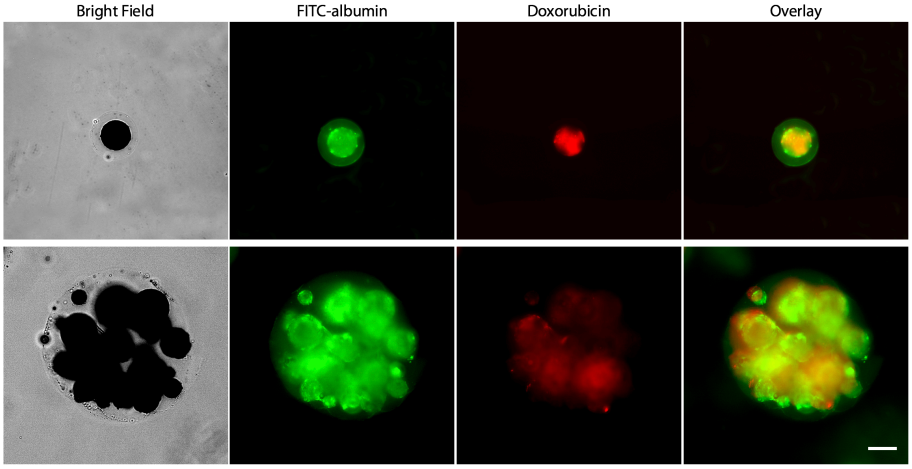

Fig. S4. Bright field and fluorescence microscopic images of the MCs confirming the successful drug loading in the MCs. Scale bar, 20 μm.

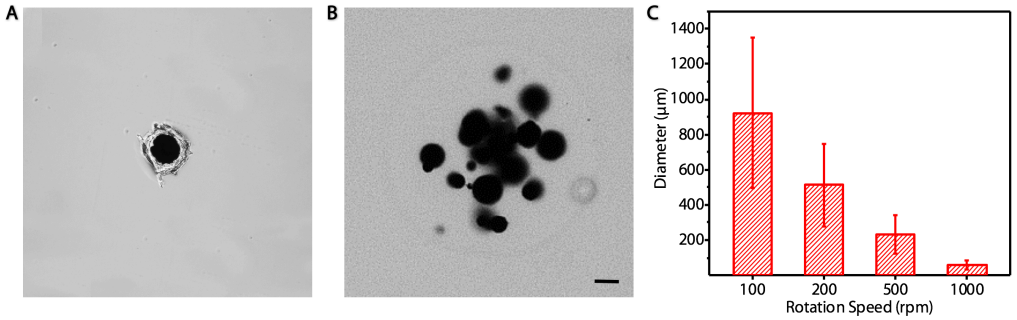

Fig. S5. Dependence of the size of the MCs on the rotation speed of magnetic stirring. (**A** and **B**) Bright field microscopic images showing MCs with different sizes. Scale bar, 20 μm. (**C**) Dependence of the diameter of the MCs on the rotation speed of magnetic stirring. Error bars represent the standard deviations (SDs) from 30 independent measurements.

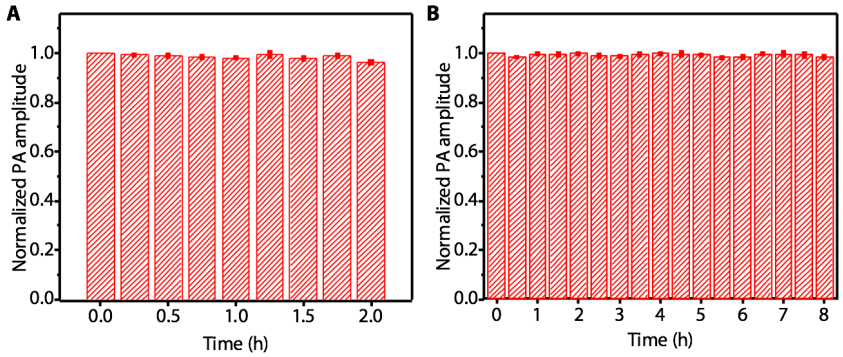

Fig. S6. Long-term stability of the PA signals of the MCs under the NIR illumination used in the PACT *in vitro* (**A**) and *in vivo* (**B**). Error bars represent the SDs from 5 independent measurements.

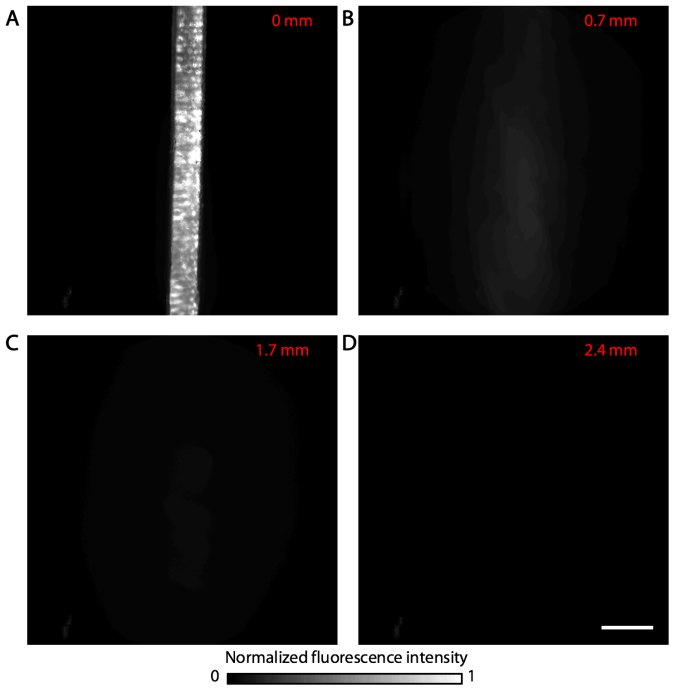

Fig. S7. Fluorescence imaging of the MCs in a silicone tube under chicken breast tissues with different depths (**A**, 0 mm; **B**, 0.7 mm; **C**, 1.7 mm; **D**, 2.4 mm). Scale bar, 1 mm.

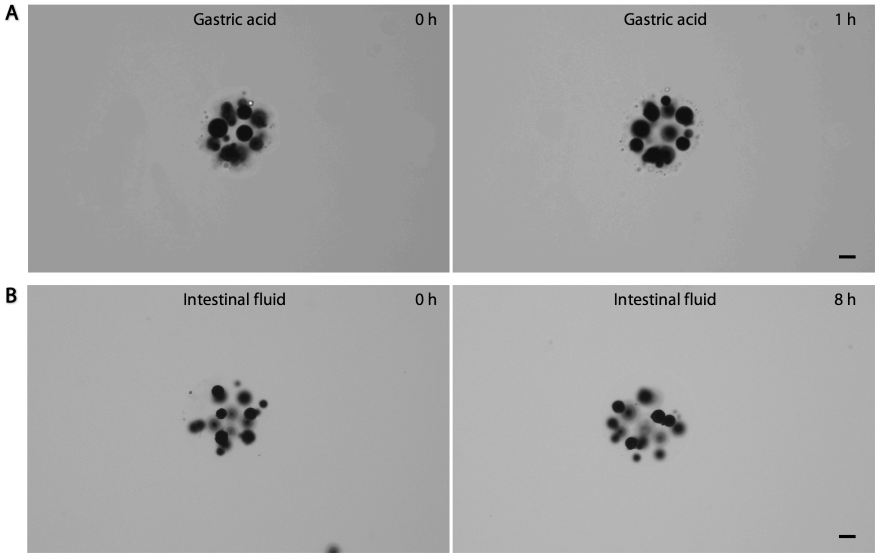

Fig. S8. Long-term structure stability of the MCs in the gastric fluid (**A**) and the intestinal fluid (**B**). Scale bars, 20 μm.

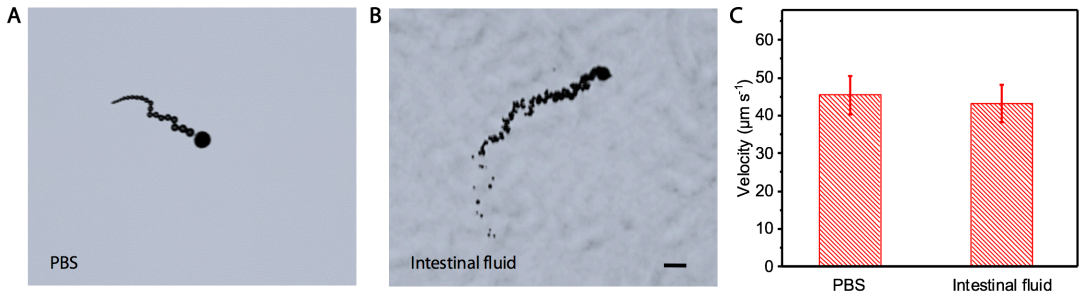

Fig. S9. Velocities of Mg-based micromotors in the different media. (**A** and **B**) Microscopic images showing the propulsion of the micromotor in PBS (**A**) and intestinal fluid (**B**), respectively. Scale bar, 20 μm. (**C**) Quantitative velocity of the micromotors in PBS and intestinal fluid. Error bars represent the SDs from 30 independent measurements.

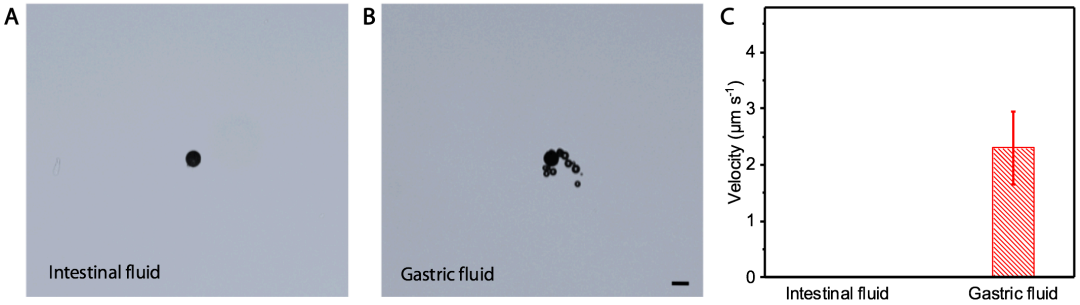

Fig. S10. Velocities of bare Mg microparticles in different media. (**A** and **B**) Microscopic images showing the behavior of an Mg microparticle in intestinal fluid (**A**) and gastric acid (**B**), respectively. Scale bar, 20 μm. (**C**) Quantitative velocities of the micromotors in intestinal fluid and gastric fluid. Error bars represent the SDs from 30 independent measurements.

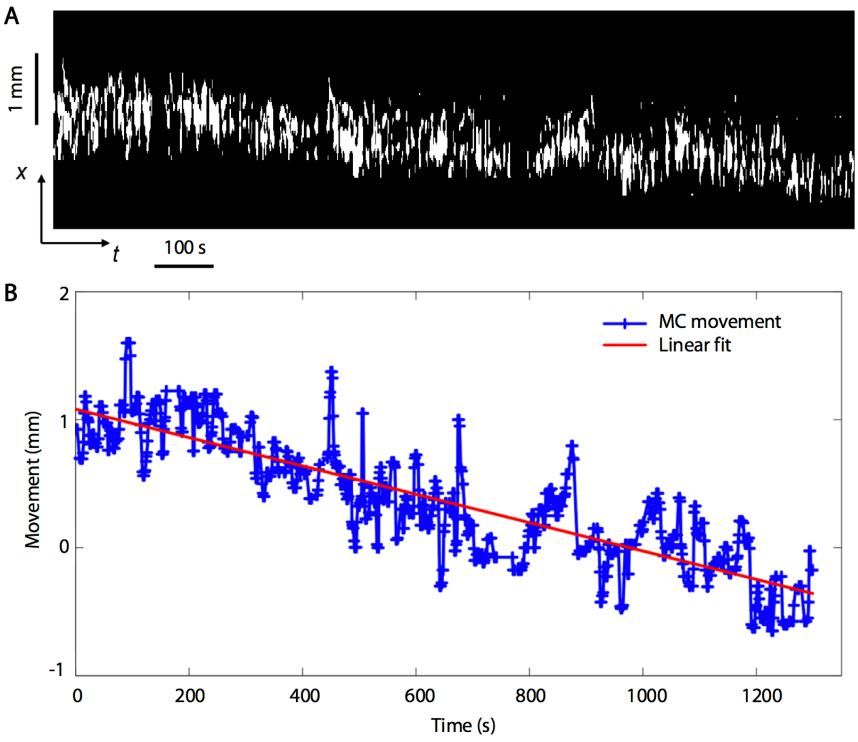

Fig. S11. Quantification of MC migration speeds. (**A**) The thresholded *x*-*t* image showing the segmented MCs at elapsed time. (**B**) The movement displacement caused by the migration of the MCs in intestines.

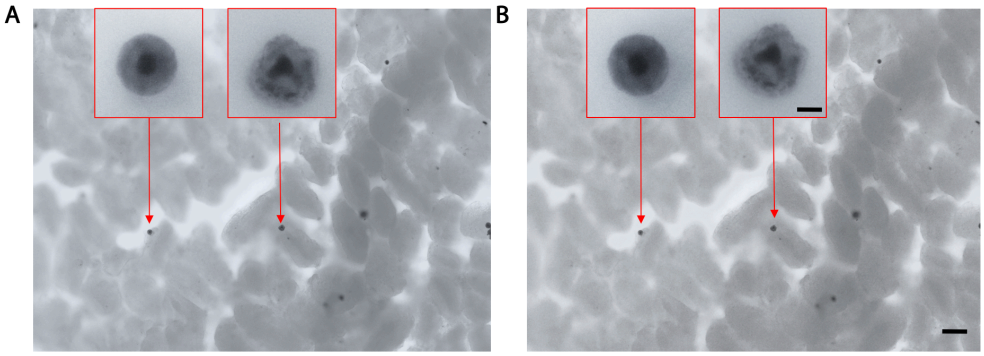

Fig. S12. Characterization of Mg dissolution in micromotors 12 hours after administration. (**A** and **B**) Microscopic images showing the micromotors attached on the intestines before (**A**) and after addition of 0.1 M gastric acid (**B**). The inset images showing enlarged micromotors. Scale bar, 100 μm; inset scale bar, 10 μm.

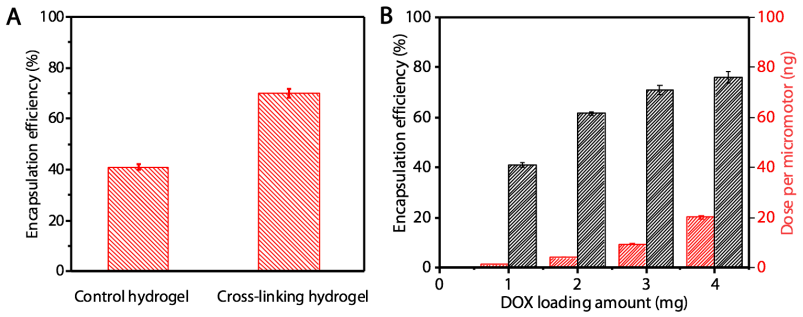

Fig. S13. Effects of cross-linking (**A**) and DOX loading amount (**B**) on the encapsulation efficiency of the micromotors and dose per micromotor. Error bars represent the SDs from 20 independent measurements.

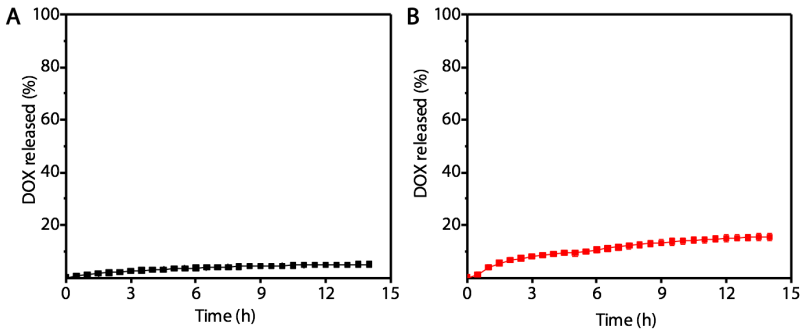

Fig. S14. Profile of DOX release from MCs (**A**) and from micromotors (**B**) as a function of time.

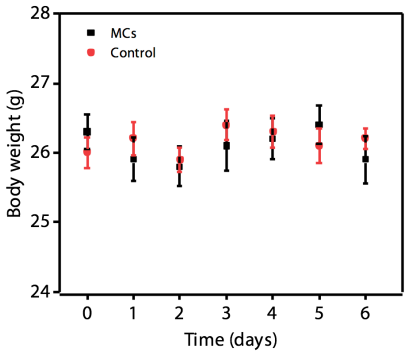

Fig. S15. The weight changes of the mice after the oral administration of the MCs and the control (DI water). Error bars represent the SDs from 5 independent measurements.